



HAL
open science

Statistical characteristics of ionospheric hiss waves

Zhiyang Xia, Lunjin Chen, Zeren Zhima, Ondřej Santolík, Richard Horne,
Michel Parrot

► **To cite this version:**

Zhiyang Xia, Lunjin Chen, Zeren Zhima, Ondřej Santolík, Richard Horne, et al.. Statistical characteristics of ionospheric hiss waves. *Geophysical Research Letters*, 2019, 46 (13), pp.7147-7156. 10.1029/2019GL083275 . insu-02157576

HAL Id: insu-02157576

<https://insu.hal.science/insu-02157576>

Submitted on 9 Sep 2019

HAL is a multi-disciplinary open access archive for the deposit and dissemination of scientific research documents, whether they are published or not. The documents may come from teaching and research institutions in France or abroad, or from public or private research centers.

L'archive ouverte pluridisciplinaire **HAL**, est destinée au dépôt et à la diffusion de documents scientifiques de niveau recherche, publiés ou non, émanant des établissements d'enseignement et de recherche français ou étrangers, des laboratoires publics ou privés.

Geophysical Research Letters

RESEARCH LETTER

10.1029/2019GL083275

Key Points:

- The ionospheric hiss wave power concentrates over a narrow frequency band with central frequency around local proton cyclotron frequency
- The ionospheric hiss power is stronger on the dayside and under higher geomagnetic activity condition and in local summer
- A ray tracing simulation demonstrates that waveguide can explain the latitudinal dependence of the ionospheric hiss narrow frequency band

Correspondence to:

Z. Xia and L. Chen,
Zhiyang.Xia@utdallas.edu;
lunjn.chen@gmail.com

Citation:

Xia, Z., Chen, L., Zhima, Z., Santolik, O., Horne, R. B., & Parrot, M. (2019). Statistical characteristics of ionospheric hiss waves. *Geophysical Research Letters*, 46, 7147–7156. <https://doi.org/10.1029/2019GL083275>

Received 11 APR 2019

Accepted 23 MAY 2019

Accepted article online 29 MAY 2019

Published online 4 JUL 2019

Corrected 8 AUG 2019

This article was corrected on 8 AUG 2019. See the end of the full text for details.

Statistical Characteristics of Ionospheric Hiss Waves

Zhiyang Xia¹ , Lunjin Chen¹ , Zeren Zhima² , Ondrej Santolik^{3,4} , Richard B. Horne⁵ , and Michel Parrot⁶ 

¹Department of Physics, University of Texas at Dallas, Richardson, TX, USA, ²Institute of Crustal Dynamics, China Earthquake Administration, Beijing, China, ³Department of Space Physics, Institute of Atmospheric Physics, Prague, Czech Republic, ⁴Faculty of Mathematics and Physics, Charles University in Prague, Prague, Czech Republic, ⁵British Antarctic Survey, Cambridge, UK, ⁶LPC2E/CNRS, Orléans, France

Abstract In this study, we use the observations of electromagnetic waves by Detection of Electromagnetic Emissions Transmitted from Earthquake Regions satellite to investigate propagation characteristics of low-altitude ionospheric hiss. In an event study, intense hiss wave power is concentrated over a narrow frequency band with a central frequency that decreases as latitude decreases, which coincides to the variation of local proton cyclotron frequency f_{CH} . The wave propagates obliquely to the background magnetic field and equatorward from high latitude region. We use about ~6 years of observations to statistically study the dependence of ionospheric hiss wave power on location, local time, geomagnetic activity, and season. The results demonstrate that the ionospheric hiss power is stronger on the dayside than nightside, under higher geomagnetic activity conditions, in local summer than local winter. The wave power is confined near the region where the local f_{CH} is equal to the wave frequency. A ray tracing simulation is performed to account for the dependence of wave power on frequency and latitude.

1. Introduction

Plasmaspheric hiss is a broadband, incoherent whistler mode wave with a typical frequency range from ~100 Hz to ~2 kHz (Meredith et al., 2004; Thorne et al., 1973), which is typically observed in the high-density regions of the plasmasphere (Dunckel & Helliwell, 1969; Russell et al., 1969; Thorne et al., 1973) and in plasmaspheric plumes (Chan & Holzer, 1976; Summers et al., 2008). It has been proposed that an embryonic source for plasmaspheric hiss is chorus waves generated outside the plasmasphere, which has been verified by both ray tracing simulations (Bortnik et al., 2008; Chum & Santolik, 2005; Santolik et al., 2006) and observations (Bortnik et al., 2009; Li, Chen, et al., 2015). Lightning-generated whistler is another potential embryonic source of plasmaspheric hiss (Green et al., 2005; Sonwalkar et al., 1989). Another generation mechanism of plasmaspheric hiss near the magnetic equator in the plasmasphere has been suggested to be linear or nonlinear wave growth theory (Chen et al., 2014; Li et al., 2013; Nakamura et al., 2016; Omura et al., 2015). Previous statistical studies have illustrated that the occurrence and the intensity of plasmaspheric hiss significantly depend on the magnetic local time and geomagnetic activity, that is, both the occurrence and the intensity are higher on the dayside and during higher levels of geomagnetic activity (Golden et al., 2012; Hartley et al., 2018; Kim et al., 2015; Li, Ma, et al., 2015).

A portion of plasmaspheric hiss (and magnetospheric chorus waves) can propagate nearly along the magnetic field lines and penetrate into the topside ionosphere as low-altitude ionospheric hiss with frequency range from 100 Hz to 1 kHz (Chen et al., 2017; Santolik et al., 2006; Santolik & Parrot, 1999), which in turn is ionospheric manifestation of magnetospheric whistler mode emissions. This serves as a mechanism to remove whistler wave field energy of plasmaspheric hiss, in addition to two other potential mechanisms, heating electrons via Landau resonance and escaping out of the plasmasphere into exohiss. The propagation features of ionospheric hiss have been studied previously. Zhima et al. (2017) reported a conjugate observation of ionospheric hiss by Detection of Electromagnetic Emissions Transmitted from Earthquake Regions (DEMETER) and plasmaspheric hiss by THEMIS, both having similar spectral properties. Case studies showed that a portion of plasmaspheric hiss emissions can propagate vertically downward in both northern and southern hemispheres to the topside ionosphere and then turns equatorward (Santolik & Parrot, 1999, 2000; Santolik et al., 2006). The mechanism of the equatorward propagation has been explained

as a waveguide formed by the magnetic field and plasma density dependence of whistler mode refractive index (Chen et al., 2017). The refractive index decreases when wave frequency approaches to the multi-ion cutoff frequency f_{cutoff} in the oxygen-rich plasma at lower altitudes (corresponding to increasing magnetic field strength) and decreases with decreasing density at higher altitude away from the topside of ionospheric density peak, which results in refractive index maximum near a few hundreds of kilometers altitude and therefore the formation of a whistler waveguide. This waveguide mechanism in the ionosphere, when at work, may result in the redistribution of the ionospheric hiss wave power in the asymmetric magnetic field in the ionosphere, especially near the South Atlantic Anomaly (SAA) region. The SAA is a weak geomagnetic field region over the south Atlantic, which is caused by the asymmetry of Earth's magnetic field with respect to the Earth's rotational axis. The inner radiation belt penetrates into the ionosphere in the SAA region and leads to the enhancement of energetic particle flux in this region. Studying wave activities in the SAA region may be potentially important for inner radiation belt dynamics (Abdu et al., 1981, 2005; Benbrook et al., 1983). The relation between ionospheric hiss and SAA will be checked in this study.

In this study, we use about 6 years of DEMETER satellite observations of waves to investigate propagation characteristics and statistical properties of ionospheric hiss emissions. In section 2, we present a case study to reveal the propagation characteristics of ionospheric hiss near the SAA region. In section 3, we analyze the dependence of ionospheric hiss wave power on location, magnetic local time, geomagnetic activity, and season. Finally, we use a ray tracing simulation to explain the observed features.

2. Ionospheric Hiss Near SAA

DEMETER was a French satellite operated by Centre National des Etudes Spatiales. It was launched in June 2004 and its mission ended in December 2010 (about 6.5 years of operating time) with a low altitude nearly Sun-synchronous circular orbit ($\sim 10:30$ and $\sim 22:30$ LT). The altitude of the spacecraft was initially 710 km and decreased to 660 km in December 2005 (Parrot et al., 2006). The Instrument Champ Electrique (Berthelier et al., 2006) consists of four sensors, which are spherical aluminum electrodes with a 60-mm diameter and deployed by stacer booms at approximately 4 m from the satellite. It can provide measurements of three components of electric field waveforms in Burst mode for the extremely low frequency (ELF) frequency channel (15–1,250 Hz), which covers the frequency range of low-altitude hiss of interest to our study. The Instrument Magnetic Search Coil (Parrot et al., 2006) can provide the Burst mode measurements of three-component magnetic field waveforms in the ELF channel. These two instruments provide the waveform measurements of six components of the electromagnetic fields to analyze the propagation and polarization properties of the observed electromagnetic waves (Santolík et al., 2006).

Figure 1 shows an event of low-altitude electromagnetic hiss emissions observed by DEMETER satellite on 15 April 2005 on the dayside (magnetic local time around 10.2) when it passed by the SAA region and triggered the Burst mode observation. This event started from $\sim 16:14$ UT and ended at $\sim 16:34$ UT (lasting about 20 min), and DEMETER was flying over the geomagnetic (dipolar) latitude λ_m from approximately 50° to -24° and the geomagnetic longitude ϕ_m from $\sim 347^\circ$ to $\sim 334^\circ$ (shown by the magenta solid line in Figure 1m). The black square, triangle, and circle symbols overplotted on the magenta line denote the start time, the end time, and the time of reaching the location of minimum background magnetic field, respectively. The colored contours in Figure 1m exhibit the variation of the local proton cyclotron frequency (f_{CH}), which is proportional to the local magnetic field strength. The local magnetic field is obtained from the International Geomagnetic Reference Field (IGRF) model. The f_{CH} contour of 300 Hz encloses the SAA region.

Using the observed six components electromagnetic waveforms and applying fast Fourier transformation, we can obtain multicomponent 6×6 spectra matrices and then determine the wave power spectral density, the ellipticity of the magnetic field polarization, the wave vector, and the Poynting vector (Santolík et al., 2010, and references within). Figures 1a and 1b show the power spectral density of the wave magnetic and electric field, respectively (the portion of electric power less than 5×10^{-6} (mV/m)²/Hz is not shown). From Figures 1a and 1b, we can see that at the high latitude (greater than $\sim 46^\circ$), there is a strong broadband emission above ~ 600 Hz. At the lower latitude, the emission becomes narrower, and the central frequency, closely following the local f_{CH} value (shown as the black dash-dot lines), decreases with decreasing latitude. After the satellite reaches the location of the minimum background magnetic field strength (marked by the black vertical dashed line), the central frequency variation starts to reverse. Figures 1c and 1d exhibit the

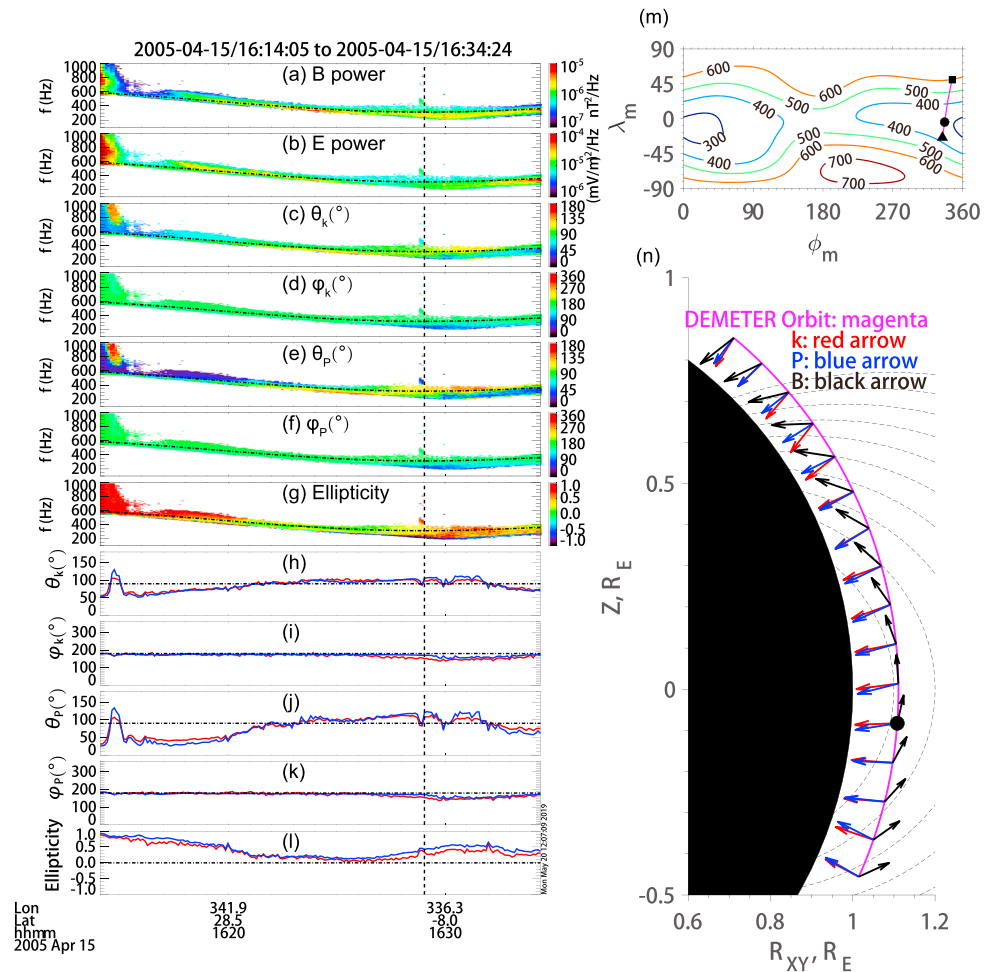


Figure 1. Ionospheric hiss event in 15 April 2005 observed by DEMETER. (a) and (b) are the wave power spectra of magnetic field and electric field. (c)–(g) are the spectra of normal angle of wave vector \mathbf{k} , azimuthal angle of \mathbf{k} , normal angle of Poynting vector \mathbf{P} , azimuthal angle of \mathbf{P} and ellipticity, respectively. (h)–(l) are the mean (red) and median (blue) values of the parameters shown in (c)–(g). (m) shows the orbit of the DEMETER (magenta line) and the contours of local f_{CH} in unit of Hz. (n) is the meridional view of the DEMETER orbit (magenta line) with the directions of \mathbf{k} (red arrows), \mathbf{P} (blue arrows), and background magnetic field \mathbf{B} (black arrows). The black dashed lines in (a)–(l) and the black circular dots in (m) and (n) represent the minimum background magnetic field point. R_{XY} denotes $(X^2 + Y^2)^{1/2}$ in the Solar magnetic coordinate system (X, Y, Z).

polar angle (θ_k) of wave vector \mathbf{k} with respect to background magnetic field and the azimuthal angle (ϕ_k) of \mathbf{k} (0° corresponds to radially outward direction from the Earth). The \mathbf{k} vector can be determined by applying singular value decomposition methods combining with Gauss's law for magnetism and Faraday's law to the electromagnetic field waveform data (Santolík et al., 2003). Figures 1e and 1f show the polar angle (θ_p) and the azimuthal angle (ϕ_p) for the Poynting vector \mathbf{P} . The polar angles of \mathbf{k} and \mathbf{P} both change from about 50° at the high latitude region to about 90° near the equator, while both the azimuthal angles of \mathbf{k} and \mathbf{P} remain around 180° (pointing toward the Earth) throughout this event. The calculated ellipticity of the magnetic field polarization (Figure 1g) shows the right-handed polarization in the high latitude region and nearly linear polarization near the equator. To show the variations of wave propagation parameters more clearly, we add the line plots of the mean (red) and median (blue) values of the polar angle of \mathbf{k} , azimuthal angle of \mathbf{k} , polar angle of \mathbf{P} , azimuthal angle of \mathbf{P} , and ellipticity in Figures 1h–1l, respectively.

Using the mean values in Figures 1h and 1k, we plot the \mathbf{k} and \mathbf{P} vectors projected onto the meridional plane in the Solar magnetic coordinate system (Figure 1n). In Figure 1n, the magenta solid line denotes the orbit of the satellite with a black solid dot marking the location of the minimum magnetic field strength. The red, blue, and black arrows represent \mathbf{k} , \mathbf{P} , and the background magnetic field (\mathbf{B}) direction vectors,

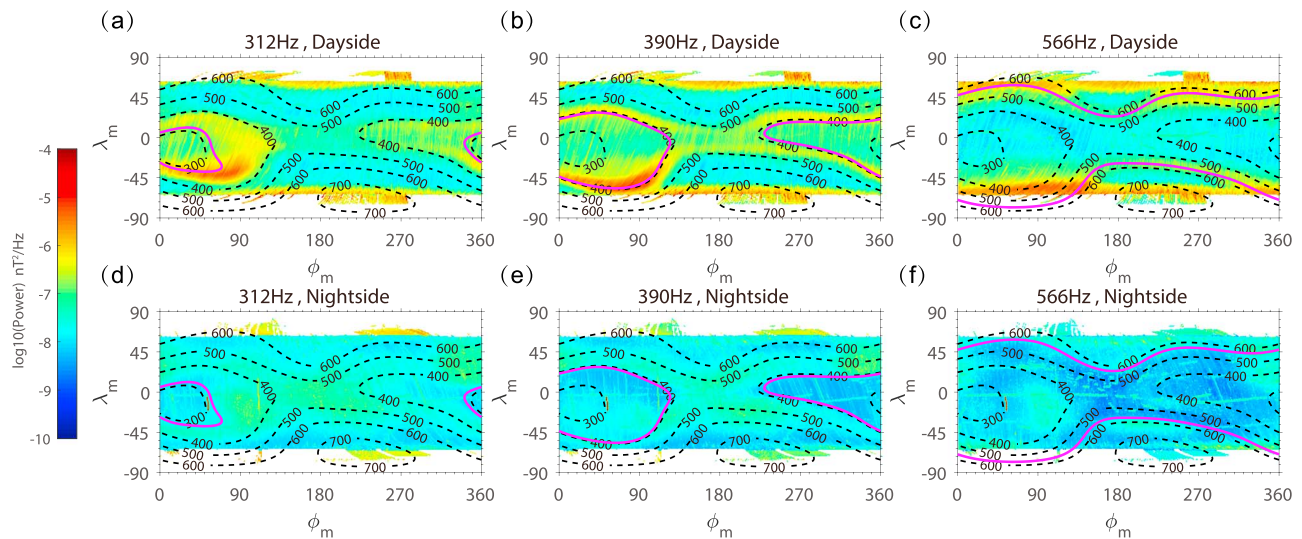


Figure 2. The global distributions of the mean value of wave magnetic field power (filled color) in geomagnetic coordinates at the DEMETER altitude for three frequency bands: 312 Hz (a,d), 390 Hz (b,e), and 566 Hz (c,f). The upper panels are for dayside, and the bottom panels are for nightside. The dashed contours stand for the distribution of the local f_{CH} at the DEMETER altitude, while the magenta lines stand for the contours where the local f_{CH} equals to the corresponding wave frequency.

respectively. The black dashed lines show the direction of background magnetic field. One can see that both \mathbf{k} and \mathbf{P} vectors point downward toward the Earth. They have southward (northward) component in the region north (south) of the minimum magnetic field location. Such latitudinal dependence of the \mathbf{k} and \mathbf{P} vector directions shows that the ionospheric hiss can propagate toward lower latitude region where the magnetic field strength is minimized.

3. Statistical Study of Hiss Power Distribution

Using about 6 years of observation from DEMETER, we perform a statistical analysis of the ionospheric hiss wave power distribution on location (geomagnetic latitude and longitude), magnetic local time, geomagnetic activity, and season. The observations of electromagnetic wave power are divided into 360 bins in geomagnetic longitude, 181 bins in geomagnetic latitude, two magnetic local times (dayside and nightside), three geomagnetic activity levels (characterized by auroral electrojet (AE) index, including $AE \leq 100$, $100 < AE \leq 300$, $AE > 300$), and four boreal seasons (spring over a range of day of year from 35 to 125, summer from 126 to 217, autumn from 218 to 308, and winter from 309 to 34 of next year). The statistical results are shown by Figures 2–4.

Figure 2 shows the global distribution of the logarithm of the average wave magnetic field power in geomagnetic longitude ϕ_m (x axis) and latitude λ_m (y axis) for two magnetic local times (dayside and nightside in upper and bottom panels, respectively) and three wave frequencies (312, 390, and 566 Hz from the left to the right). The dashed black contours represent the spatial variation of local f_{CH} , which is obtained from the IGRF model. The f_{CH} contours of values equal to the three wave frequencies are also plotted as the magenta solid contours for reference, from the left to right panels.

Comparing the wave power between the upper and lower panels, we can see that the ionospheric hiss at all the three frequencies is 2–3 orders of magnitude more intense on the dayside than nightside. This day-night distribution feature of ionospheric hiss is similar to that of the plasmaspheric hiss (Golden et al., 2012; Hartley et al., 2018; Kim et al., 2015; Li, Ma, et al., 2015), which is consistent with the proposed idea (Chen et al., 2017) that the ionospheric hiss originates primarily from the whistler mode plasmaspheric hiss. Such local time distribution of the ionospheric hiss with weaker intensity at nightside also excludes the possibility of electromagnetic sources below the ionosphere (such as lightning activities), because the collisional damping of whistler mode is stronger on the dayside than nightside.

By examining wave power distribution on the dayside (Figure 2, upper panels), one can see a strong dependence of the spatial distribution on wave frequency. The wave power at 312 Hz has the strongest power

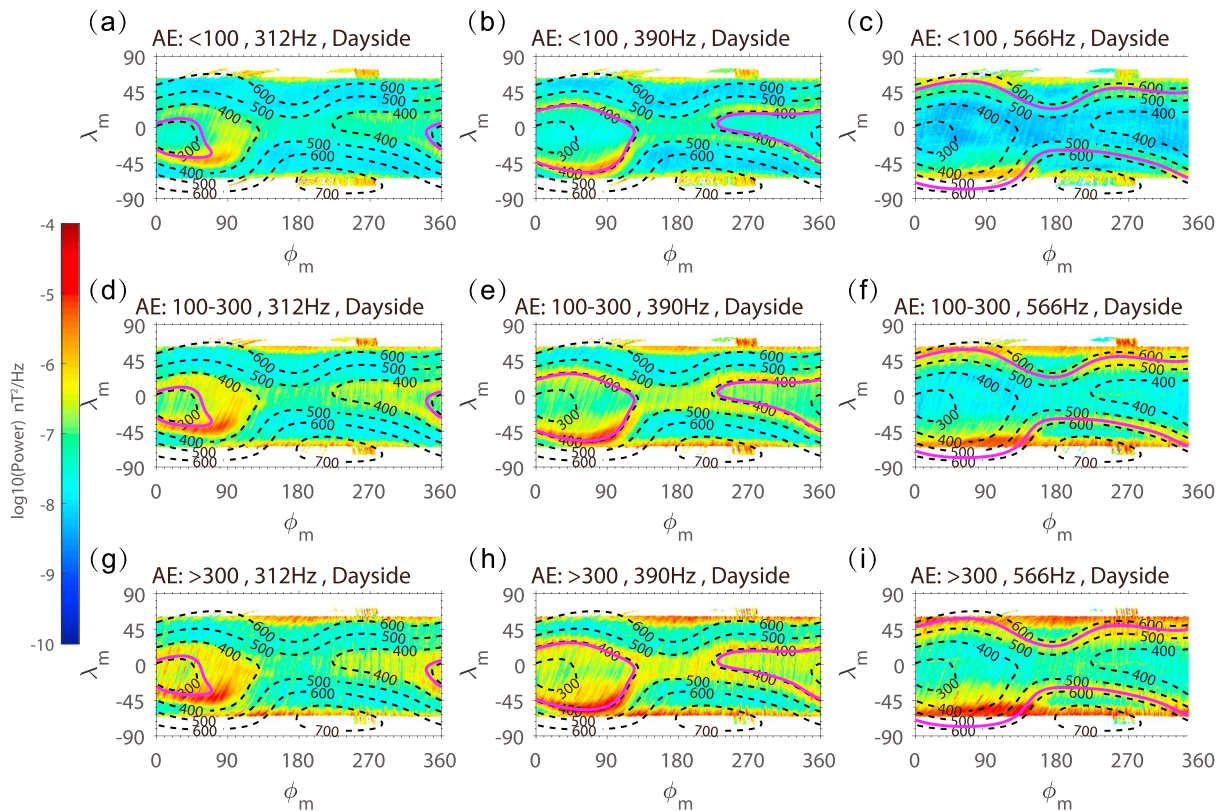


Figure 3. Wave power distribution in geomagnetic coordinates on the dayside for the same frequencies as Figure 2 and under three different geomagnetic activity levels: $AE \leq 100$ (top), $100 < AE \leq 300$ (middle), and $AE > 300$ (bottom).

just outside the region where local proton cyclotron frequency is close to that frequency and around the SAA region (Figure 2a). As wave frequency increases, the region with strong wave power moves toward the higher latitude region. It should be noted that, for all three frequencies, there is a secondary band of intense wave power at relatively high latitude near 60° . For smaller frequencies (Figures 2a and 2b), the low-latitude band tracks f_{CH} fairly well and is separated from the high-latitude band. For higher frequency (Figure 2c), the two bands merge near the magnetic longitude of SAA, while remain separated away the SAA (over the range of ϕ_m from $\sim 150^\circ$ to $\sim 250^\circ$), where the proximity of the low-latitude band frequency near f_{CH} is still noticeable. We will explain this frequency dependence in next section.

Figure 3 shows the distribution of average power spectral density on the dayside for the same three different frequencies as Figure 2 under three different geomagnetic activity levels (top: $AE \leq 100$, middle: $100 < AE \leq 300$, and bottom: $AE > 300$). One can see that the ionospheric hiss power shows significant dependence on the geomagnetic activity level. Power spectral density at all the frequencies of both lower and upper latitude bands is enhanced under higher AE index condition. Such geomagnetic activity dependence of ionospheric hiss is consistent with the idea of plasmaspheric hiss as its source, since plasmaspheric hiss wave amplitude increases under higher geomagnetic activity levels (Golden et al., 2012; Hartley et al., 2018; Kim et al., 2015; Li, Ma, et al., 2015).

The seasonal dependence of ionospheric wave power is shown by Figure 4. Figures 4a–4d show the distributions of ionospheric wave power spectral densities at 312 Hz on the dayside for the four seasons. Since the season is determined by geographic location, this distribution is mapped in the geographic coordinates. Two red dashed contours corresponding to local f_{CH} equaling to 302 and 362 Hz are added. The wave power in the region enclosed by the two red dashed contours in the southern hemisphere is strong and shows significant seasonal dependence with strongest intensity in local summer (Figure 4d, boreal winter) and weakest intensity in local winter (Figure 4b, boreal summer). To confirm this seasonal dependence, we calculate the mean wave power in the region between the two red dashed contours in the southern hemisphere and plot its annual variation as the red solid line in Figure 4e. The result indicates that the mean wave power varies

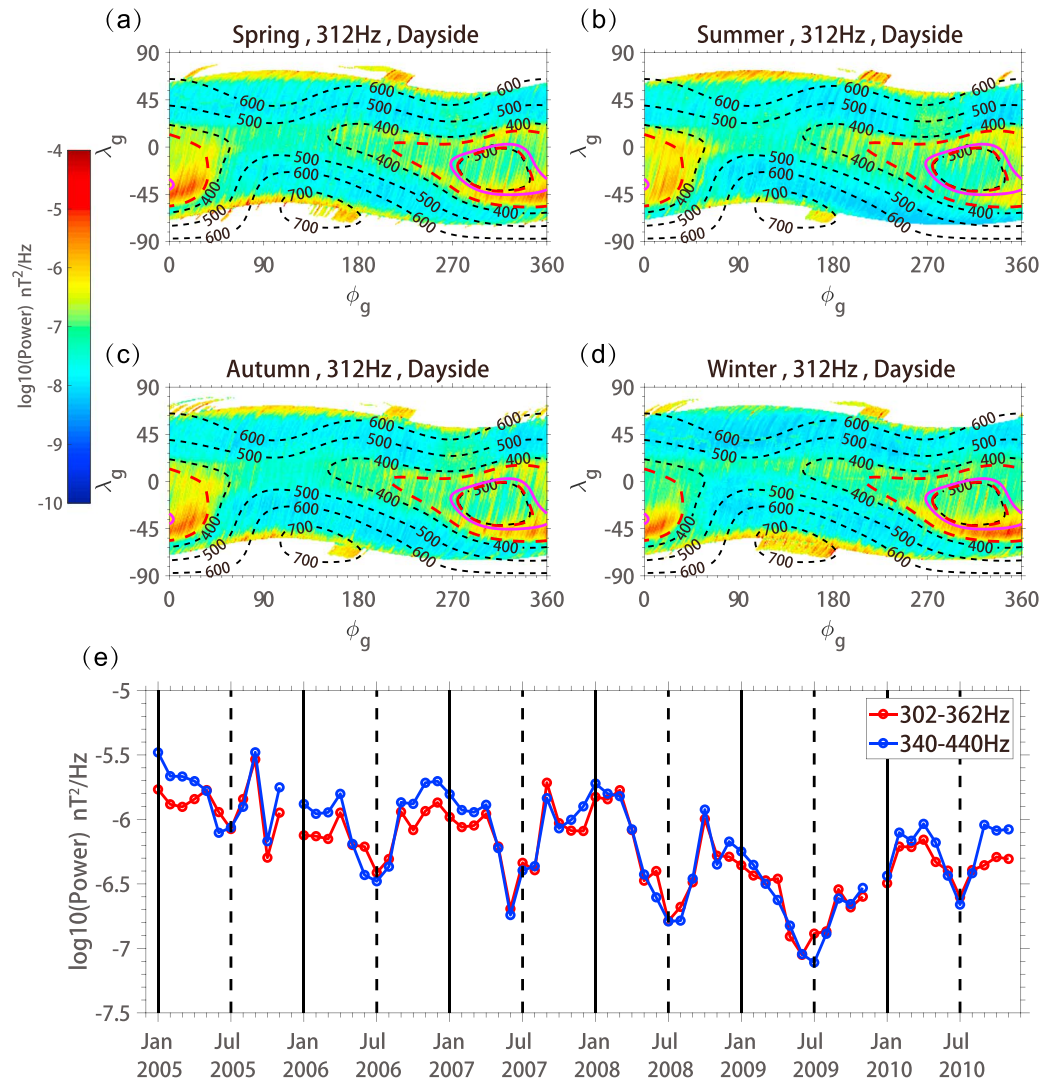


Figure 4. Wave power distribution in geographic coordinates on the dayside for 312-Hz frequency and four boreal seasons: (a) Spring (day of year [doy]: 35 to 125), (b) Summer (doy: 126 to 217), (c) Autumn (doy: 218 to 308), and (d) Winter (doy: 309 to 34). (e) shows the annual variations of the mean values of 312-Hz wave power inside the region with local f_{CH} between 302 and 362 Hz (red line) and 390-Hz wave power inside the region with local f_{CH} between 340 and 440 Hz (blue line). The gaps in December in 2005 and 2009 are due to lack of data.

periodically with minimum values near July (local winter) and maximum values near January (local summer), where the maximum to the minimum ratio is on the order of $10^{1/2}$ – 10^1 . We also check the mean power for 390-Hz wave in the region with local f_{CH} between 340 and 440 Hz in the southern hemisphere and plot its variation as the blue line in Figure 4e. The mean power of 390-Hz wave shows similar annual variation as that of the 312-Hz wave. Thus, we conclude that the power of ionospheric hiss wave is stronger in local summer than in local winter. Meredith et al. (2006), however, have indicated that the intensity of low frequency (<2 kHz) plasmaspheric hiss is strongest at equinoxes. Possible explanation for the seasonal dependence of the ionospheric hiss intensity is through the seasonal variation of the f_{cutoff} , which is determined by the local ion composition. In local summer, the ion composition is dominated by O^+ around the altitude of DEMETER orbit and f_{cutoff} nearly equals to f_{CH} . In local winter, O^+ concentration decreases significantly (refer to the International Reference Ionosphere model; Bilitza, 2018) and leads f_{cutoff} significantly smaller than f_{CH} . Thus, for a given wave frequency, wave reflection (where wave frequency is near f_{cutoff}) takes place at lower altitudes in local winter than in local summer, leading to more attenuation because of longer propagation path and enhanced damping rate. It is also interesting to point out, from Figure 4e, that ionospheric hiss

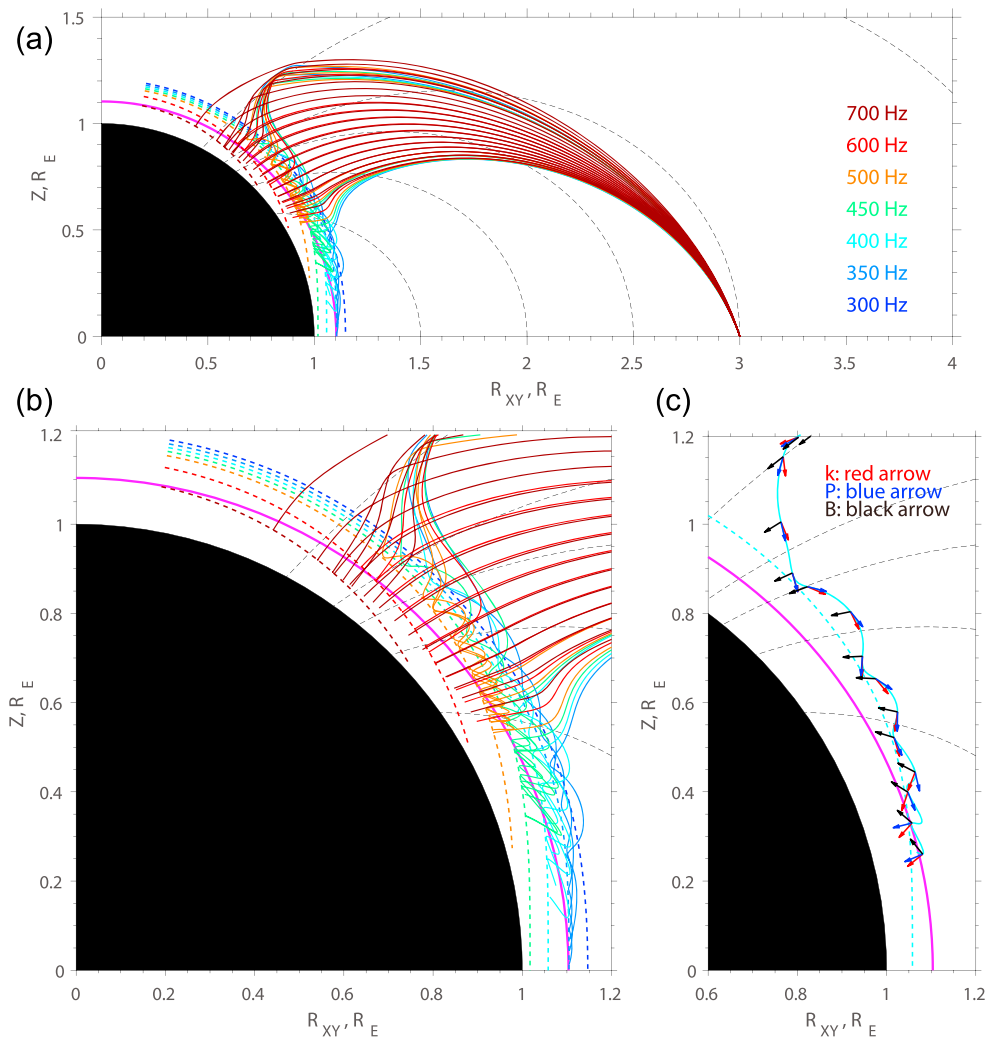


Figure 5. Ray tracing model results of waves originating at $L = 3$ for different frequencies (300–700 Hz) and initial wave normal angles (9° to 90°) shown in a meridional plane. Only ray paths that reach the ionospheric altitude are shown. Colored solid lines represent the wave propagation paths, and the colored dashed lines stand for the locations where local f_{cutoff} equaling to the corresponding wave frequency (color-coded). The magenta solid line shows the orbit of the DEMETER satellite, and the black dashed lines are the background magnetic field lines. (b) is the zoom-in plot of (a) in the ionospheric region. (c) shows the directions of \mathbf{k} , \mathbf{P} , and \mathbf{B} at several selected points of a ray with 400-Hz wave frequency.

wave intensity reached a minimum in 2009, which is the year of solar minimum in solar cycle 23. This solar cycle dependence is also consistent with that of plasmaspheric hiss (Golden et al., 2011).

4. Ray Tracing Model Analysis

In section 3, we have demonstrated the dependence of ionospheric hiss wave power on magnetic local time and geomagnetic activity. This dependence is consistent with the theory that the ionospheric hiss originates primarily from the plasmaspheric hiss, as discussed above. The frequency dependence of spatial distribution of ionospheric hiss wave power can also be explained by propagation mechanism of whistler-mode emission from the magnetosphere into the ionosphere and inside the ionosphere. This propagation mechanism has been demonstrated by Chen et al. (2017). A portion of broadband plasmaspheric hiss waves can propagate nearly along magnetic field lines into the topside ionosphere at high latitude regions as type I ionospheric hiss with broadband spectra. Then the type I ionospheric hiss turns equatorward and evolves into type II ionospheric hiss with a narrow frequency band near local proton cyclotron frequency (as the event shown in Figure 1). The narrowband type II emission was explained as waveguide, as demonstrated below.

We use the same HOTRAY ray tracing code (Horne, 1989) as that used in Chen et al. (2017) with a dipole magnetic field and a diffusive equilibrium plasma density model (Bortnik et al., 2011, and references within). We adopt as our source plasmaspheric hiss waves located at the equator of $L = 3$. The source wave frequency varies from 300 to 700 Hz, and the initial wave normal angle varies from 9° to 90° . Ray tracing is terminated when the wavelength is comparable to spatial scale of background field and plasma variations. Only ray paths of those waves that penetrate into the ionospheric altitude (~ 700 km) are shown in Figure 5a. A zoom-in view near the ionosphere is shown in Figure 5b. Different colored solid lines represent the wave paths for different frequencies, and the colored dashed lines denote the contours of local f_{cutoff} equaling to corresponding wave frequencies. The black dashed lines show the topology of dipole field lines, and the magenta solid line indicates the altitude of DEMETER satellite. Figure 5c shows the directions of \mathbf{k} (red arrow), \mathbf{P} (blue arrow), and \mathbf{B} (black arrow) at several selected points of a ray with 400-Hz wave frequency. Both \mathbf{k} and \mathbf{P} vectors are directed downward and equatorward at low latitudes and are nearly perpendicular to the background magnetic field, which is consistent with the observational results in Figure 1. From Figure 5, we can see that the hiss waves penetrate into the ionosphere at high latitudes ($\sim 25^\circ$ to $\sim 60^\circ$) almost vertically downward along the magnetic field lines. When reaching the corresponding f_{cutoff} lines at the ionospheric altitude, ray paths of different frequencies start to separate. The waves with lower frequencies reflect upward at higher altitude region and are trapped inside the waveguide to propagate equatorward, while the higher frequency waves enter the waveguide at lower altitude. Because waveguide places lower and upper altitude limits for those waves, the waves can be only seen over a limited range of latitude at a fixed altitude. Therefore, such frequency-dependent waveguide propagation not only explains why the ionospheric hiss at low latitude region is observed by DEMETER (e.g., Figure 1) with a narrow frequency band but also explains why this band is near local proton cyclotron frequency (which is close to f_{cutoff} at DEMETER altitude) and why the central frequency tends to decrease with decreasing latitude.

For more realistic IGRF geomagnetic field, the minimum magnetic field surface is not necessarily the magnetic equator, especially around the SAA region. For the individual event shown Figure 1, the minimum magnetic field exists in the SAA region, and the hiss waves from both northern and southern hemispheres eventually propagate into the SAA region. The statistical results in section 3 support that SAA region is favorable to trap ionospheric hiss waves of 400 Hz and below (Figure 3, the left and middle columns), while the waves at higher frequencies can be trapped at all magnetic longitudes.

5. Conclusions and Discussion

In this paper, we present a case study from DEMETER satellite observations near the SAA region to understand wave propagation features of ionospheric hiss. Then we use about 6 years of observations of DEMETER satellite to undertake a statistical study of the wave power distribution of ionospheric hiss on location (geomagnetic latitude and longitude), magnetic local time (day and night), geomagnetic activity, and season. A ray tracing model simulation is also applied to explain the latitudinal dependence of wave frequency band. The main conclusions of this study are summarized as the following.

1. In the case study, the intense hiss wave power concentrates over a narrow frequency band that decreases from about ~ 600 Hz at the high latitude region to ~ 300 Hz near the equator, which coincides to the variation of local proton cyclotron frequency f_{CH} . The waveform measurement shows that the wave propagates obliquely to the background magnetic field and equatorward from high latitude region.
2. The low-altitude ionospheric hiss power tends to be stronger on the dayside than nightside, and under higher geomagnetic activity conditions. Those characteristics are consistent with the distribution of plasmaspheric hiss. The ionospheric hiss power shows seasonal variation with stronger power in local summer than in local winter.
3. The wave power is confined near the region where the local proton cyclotron frequency f_{CH} is near the wave frequency. This is caused by the propagation within a waveguide structure formed by the variation of plasma density and cutoff frequency.
4. A ray tracing simulation demonstrates that waveguide can explain the latitudinal dependence and narrowness of the ionospheric hiss frequency band.

Emissions that can reach the ionospheric altitude will redistribute the wave energy according to wave frequency through frequency-dependent waveguide in the topside ionosphere, resulting in that the waves at low latitude region are found with wave frequency near local proton cyclotron frequency. Our statistical analysis not only reveals such frequency-dependent characteristics but also demonstrates the dependence

of ionospheric hiss wave power on local time, geomagnetic activity, and season. All those statistical results support the proposed idea that those emissions originate primarily from the plasmaspheric hiss.

Because of frequency-dependent propagation, the lower frequency waves (below 400 Hz) are trapped only near SAA region, while the upper frequency waves are trapped at all magnetic longitudes. How important these waves near SAA are in facilitating the precipitation loss remains to be found out.

Acknowledgments

We acknowledge the DEMETER scientific mission for providing data (<http://demeter.cnrs-orleans.fr/>). This research was supported by the NSF grant AGS 1702805 through the Geospace Environment Modeling program and the AFOSR grant of FA9550-16-1-0344. Zeren Zhima acknowledges the support of NSFC grant 41574139/41874174. Ondrej Santolík acknowledges support from the Czech Academy of Sciences through the Praemium Academiae award. Richard B. Horne is supported by NERC Highlight Topic GrantNE/P01738X/1 (Rad-Sat).

References

Abdu, M. A., Batista, I. S., Carrasco, A. J., & Brum, C. G. M. (2005). South Atlantic magnetic anomaly ionization: A review and a new focus on electrodynamic effects in the equatorial ionosphere. *Journal of Atmospheric and Solar-Terrestrial Physics*, 67(17), 1643–1657. <https://doi.org/10.1016/j.jastp.2005.01.014>

Abdu, M. A., Batista, I. S., Piazza, L. R., & Massambani, O. (1981). Magnetic storm associated enhanced particle precipitation in the South Atlantic Anomaly: Evidence from VLF phase measurements. *Journal of Geophysical Research*, 86(A9), 7533–7542. <https://doi.org/10.1029/JA086iA09p07533>

Benbrook, J. R., Bering, E. A. III, Leverenz, H., Roeder, J. L., & Sheldon, W. R. (1983). Quiet-time electron precipitation at L = 4 in the South Atlantic Anomaly. *Journal of Geophysical Research*, 88(A1), 189–199. <https://doi.org/10.1029/JA088iA01p00189>

Berthelier, J., Godefroy, M., Leblanc, F., Malingre, M., Menvielle, M., Lagoutte, D., et al. (2006). ICE, the electric field experiment on DEMETER. *Planetary and Space Science*, 54(5), 456–471. <https://doi.org/10.1016/j.pss.2005.10.016>

Bilitza, D. (2018). IRI the International Standard for the Ionosphere. *Advances in Radio Science*, 16, 1–11. <https://doi.org/10.5194/ars-16-1-2018>

Bortnik, J., Chen, L., Li, W., Thorne, R. M., & Horne, R. B. (2011). Modeling the evolution of chorus waves into plasmaspheric hiss. *Journal of Geophysical Research*, 116, A08221. <https://doi.org/10.1029/2011JA016499>

Bortnik, J., Li, W., Thorne, R. M., Angelopoulos, V., Cully, C., Bonnell, J., et al. (2009). An observation linking the origin of plasmaspheric hiss to discrete chorus emissions. *Science*, 324(5928), 775–778. <https://doi.org/10.1126/science.1171273>

Bortnik, J., Thorne, R. M., & Meredith, N. P. (2008). The unexpected origin of plasmaspheric hiss from discrete chorus waves. *Nature*, 452, 62–66. <https://doi.org/10.1038/nature06741>

Chan, K.-W., & Holzer, R. E. (1976). ELF hiss associated with plasma density enhancements in the outer magnetosphere. *Journal of Geophysical Research*, 81(13), 2267–2274. <https://doi.org/10.1029/JA081i013p02267>

Chen, L., Santolík, O., Hajoš, M., Zheng, L., Zhima, Z., Heelis, R., et al. (2017). Source of the low-altitude hiss in the ionosphere. *Geophysical Research Letters*, 44, 2060–2069. <https://doi.org/10.1002/2016GL072181>

Chen, L., Thorne, R. M., Bortnik, J., Li, W., Horne, R. B., Reeves, G. D., et al. (2014). Generation of unusually low frequency plasmaspheric hiss. *Geophysical Research Letters*, 41, 5702–5709. <https://doi.org/10.1002/2014GL060628>

Chum, J., & Santolík, O. (2005). Propagation of whistler-mode chorus to low altitudes: Divergent ray trajectories and ground accessibility. *Annals of Geophysics*, 23(12), 3727–3738. <https://doi.org/10.5194/angeo-23-3727-2005>

Dunckel, N., & Helliwell, R. A. (1969). Whistler-mode emissions on the OGO 1 satellite. *Journal of Geophysical Research*, 74, 6371–6385. <https://doi.org/10.1029/JA074i026p06371>

Golden, D. I., Spasojevic, M., & Inan, U. S. (2011). Determination of solar cycle variations of midlatitude ELF/VLF chorus and hiss via automated signal detection. *Journal of Geophysical Research*, 116, A03225. <https://doi.org/10.1029/2010JA016193>

Golden, D. I., Spasojevic, M., Li, W., & Nishimura, Y. (2012). Statistical modeling of plasmaspheric hiss amplitude using solar wind measurements and geomagnetic indices. *Geophysical Research Letters*, 39, L06103. <https://doi.org/10.1029/2012GL051185>

Green, J. L., Boardsen, S., Garcia, L., Taylor, W. W. L., Fung, S. F., & Reinisch, B. W. (2005). On the origin of whistler mode radiation in the plasmasphere. *Journal of Geophysical Research*, 110, A03201. <https://doi.org/10.1029/2004JA010495>

Hartley, D. P., Kletzing, C. A., Santolík, O., Chen, L., & Horne, R. B. (2018). Statistical properties of plasmaspheric hiss from Van Allen Probes observations. *Journal of Geophysical Research: Space Physics*, 123, 2605–2619. <https://doi.org/10.1002/2017JA024593>

Horne, R. B. (1989). Path-integrated growth of electrostatic waves: The generation of terrestrial myriametric radiation. *Journal of Geophysical Research*, 94(A7), 8895–8909. <https://doi.org/10.1029/JA094iA07p08895>

Kim, K.-C., Lee, D.-Y., & Shprits, Y. (2015). Dependence of plasmaspheric hiss on solar wind parameters and geomagnetic activity and modeling of its global distribution. *Journal of Geophysical Research: Space Physics*, 120, 1153–1167. <https://doi.org/10.1002/2014JA020687>

Li, W., Chen, L., Bortnik, J., Thorne, R. M., Angelopoulos, V., Kletzing, C. A., et al. (2015). First evidence for chorus at a large geocentric distance as a source of plasmaspheric hiss: Coordinated THEMIS and Van Allen Probes observation. *Geophysical Research Letters*, 42, 241–248. <https://doi.org/10.1002/2014GL062832>

Li, W., Ma, Q., Thorne, R. M., Bortnik, J., Kletzing, C. A., Kurth, W. S., et al. (2015). Statistical properties of plasmaspheric hiss derived from Van Allen Probes data and their effects on radiation belt electron dynamics. *Journal of Geophysical Research: Space Physics*, 120, 3393–3405. <https://doi.org/10.1002/2015JA021048>

Li, W., Thorne, R. M., Bortnik, J., Reeves, G. D., Kletzing, C. A., Kurth, W. S., et al. (2013). An unusual enhancement of low-frequency plasmaspheric hiss in the outer plasmasphere associated with substorm-injected electrons. *Geophysical Research Letters*, 40, 3798–3803. <https://doi.org/10.1002/grl.50787>

Meredith, N. P., Horne, R. B., Clilverd, M. A., Horsfall, D., Thorne, R. M., & Anderson, R. R. (2006). Origins of plasmaspheric hiss. *Journal of Geophysical Research*, 111, A09217. <https://doi.org/10.1029/2006JA011707>

Meredith, N. P., Horne, R. B., Thorne, R. M., Summers, D., & Anderson, R. R. (2004). Substorm dependence of plasmaspheric hiss. *Journal of Geophysical Research*, 109, A06209. <https://doi.org/10.1029/2004JA010387>

Nakamura, S., Omura, Y., Summers, D., & Kletzing, C. A. (2016). Observational evidence of the nonlinear wave growth theory of plasmaspheric hiss. *Geophysical Research Letters*, 43, 10040–10049. <https://doi.org/10.1002/2016GL070333>

Omura, Y., Nakamura, S., Kletzing, C. A., Summers, D., & Hikishima, M. (2015). Nonlinear wave growth theory of coherent hiss emissions in the plasmasphere. *Journal of Geophysical Research: Space Physics*, 120, 7642–7657. <https://doi.org/10.1002/2015JA021520>

Parrot, M., Benoist, D., Berthelier, J. J., Błęcki, J., Chapuis, Y., Colin, F., et al. (2006). The magnetic field experiment IMSC and its data processing onboard DEMETER: Scientific objectives, description and first results. *Planetary and Space Science*, 54(5), 441–455. <https://doi.org/10.1016/j.pss.2005.10.015>

- Russell, C. T., Holzer, R. E., & Smith, E. J. (1969). Ogo 3 observations of elf noise in the magnetosphere: 1. Spatial extent and frequency of occurrence. *Journal of Geophysical Research*, *74*(3), 755–777. <https://doi.org/10.1029/JA074i003p00755>
- Santolik, O., Chum, J., Parrot, M., Gurnett, D. A., Pickett, J. S., & Cornilleau-Wehrlin, N. (2006). Propagation of whistler mode chorus to low altitudes: Spacecraft observations of structured ELF hiss. *Journal of Geophysical Research*, *A10208*. <https://doi.org/10.1029/2005JA011462>
- Santolik, O., Němeca, F., Parrot, M., Lagoutteb, D., Madriab, L., & Bertheliecr, J. J. (2006). Analysis methods for multi-component wave measurements on board the DEMETER spacecraft. *Planetary and Space Science*, *54*(5), 512–527. <https://doi.org/10.1016/j.pss.2005.10.020>
- Santolik, O., & Parrot, M. (1999). Case studies on the wave propagation and polarization of ELF emissions observed by Freja around the local proton gyrofrequency. *Journal of Geophysical Research*, *104*(A2), 2459–2475. <https://doi.org/10.1029/1998JA900045>
- Santolik, O., & Parrot, M. (2000). Application of wave distribution function methods to an ELF hiss event at high latitudes. *Journal of Geophysical Research*, *105*(A8), 18885–18894. <https://doi.org/10.1029/2000JA900029>
- Santolik, O., Parrot, M., & Lefeuvre, F. (2003). Singular value decomposition methods for wave propagation analysis. *Radio Science*, *38*(1), 1010. <https://doi.org/10.1029/2000RS002523>
- Santolik, O., Pickett, J. S., Gurnett, D. A., Menietti, J. D., Tsurutani, B. T., & Verkhoglyadova, O. (2010). Survey of Poynting flux of whistler mode chorus in the outer zone. *Journal of Geophysical Research*, *115*, A00F13. <https://doi.org/10.1029/2009JA014925>
- Sonwalkar, V. S., Inan, U. S. (1989). Lightning as an embryonic source of VLF hiss. *Journal of Geophysical Research*, *94*, 6986–6994. <https://doi.org/10.1029/JA094iA06p06986>
- Summers, D., Ni, B., Meredith, N. P., Richard, H., Thorne, M., Moldwin, M. B., & Anderson, R. R. (2008). Electron scattering by whistler-mode ELF hiss in plasmaspheric plumes. *Journal of Geophysical Research*, *113*, A04219. <https://doi.org/10.1029/2007JA012678>
- Thorne, R. M., Smith, E. J., Burton, R. K., & Holzer, R. E. (1973). Plasmaspheric hiss. *Journal of Geophysical Research*, *78*(10), 1581–1596. <https://doi.org/10.1029/JA078i010p01581>
- Zhima, Z., Chen, L., Xiong, Y., Cao, J., & Fu, H. (2017). On the origin of ionospheric hiss: A conjugate observation. *Journal of Geophysical Research: Space Physics*, *122*, 11784–11793. <https://doi.org/10.1002/2017JA024803>

Erratum

In the originally published version of this article, NSF grant AGS 1702805 appeared incorrectly in the Acknowledgments as NSF grant 1705079; also, in the first paragraph of the Introduction, "hiss" wrongly appeared as "hsiss" in one sentence. These errors have since been corrected, and the present version may be considered the authoritative version of record.